Journal of Geophysical Research: Oceans

RESEARCH ARTICLE
10.1002/2015JC011320

Key Points:
- Roll vortices are the prevalent eddy circulations in the atmospheric boundary layer of hurricanes
- Atmospheric roll vortices can have a profound impact on oil operation and oil spill transport
- Dynamic and convective instability of roll generation depends strongly on the storm-induced cooling

Correspondence to:
P. Zhu,
zhup@fiu.edu

Impact of storm-induced cooling of sea surface temperature on large turbulent eddies and vertical turbulent transport in the atmospheric boundary layer of Hurricane Isaac

Ping Zhu[1], Yuting Wang[2,3], Shuyi S. Chen[4], Milan Curcic[4], and Cen Gao[1]

[1]Department of Earth and Environment, Florida International University, Miami, Florida, USA, [2]School of Earth Sciences, Zhejiang University, Hangzhou, Zhejiang, China, [3]Chinese Academy of Meteorological Science, Beijing, China, [4]Rosenstiel School of Marine and Atmospheric Science, University of Miami, Coral Gables, Florida, USA

Abstract Roll vortices in the atmospheric boundary layer (ABL) are important to oil operation and oil spill transport. This study investigates the impact of storm-induced sea surface temperature (SST) cooling on the roll vortices generated by the convective and dynamic instability in the ABL of Hurricane Isaac (2012) and the roll induced transport using hindcasting large eddy simulations (LESs) configured from the multiply nested Weather Research & Forecasting model. Two experiments are performed: one forced by the Unified Wave INterface - Coupled Model and the other with the SST replaced by the NCEP FNL analysis that does not include the storm-induced SST cooling. The simulations show that the roll vortices are the prevalent eddy circulations in the ABL of Isaac. The storm-induced SST cooling causes the ABL stability falls in a range that satisfies the empirical criterion of roll generation by dynamic instability, whereas the ABL stability without considering the storm-induced SST cooling meets the criterion of roll generation by convective instability. The ABL roll is skewed and the increase of convective instability enhances the skewness. Large convective instability leads to large vertical transport of heat and moisture; whereas the dominant dynamic instability results in large turbulent kinetic energy but relatively weak heat and moisture transport. This study suggests that failure to consider roll vortices or incorrect initiation of dynamic and convective instability of rolls in simulations may substantially affect the transport of momentum, energy, and pollutants in the ABL and the dispersion/advection of oil spill fume at the ocean surface.

1. Introduction

It has long been recognized that the turbulent flow in the atmospheric boundary layer (ABL) is not totally chaotic. Often, there exist organized eddy circulations that have well defined structures. One of them is the horizontal streamwise roll vortices, which can be best visualized by the so-called cloud streets, a phenomenon commonly seen in photographs taken from airplanes and high resolution satellite images. Roll vortices observed in fair-weather conditions can have a range of scales varying from 1 to 2 km in depth (equivalent to the depth of ABL), from 2 to 20 km in wavelength, and from 10 to 1000 km in downstream extension [*Etling and Brown*, 1993].

ABL roll vortices can be generated by both dynamic and convective instabilities. One of the dynamic instability modes is the so-called inflection-point instability, which was named after the inflection-point existing in the cross-wind profile of the ABL. As an illustration, Figure 1 shows the simplest Ekman-flow (with a constant eddy viscosity) in a coordinate with x axis aligned with the downwind direction of the mean flow. An inflection-point is clearly shown in the cross-wind profile, which coincides with the maximum of cross-wind vorticity. *Faller and Kaylor* [1966] first showed that the neutral barotropic Ekman-flow with an inflection-point is inherently unstable to small perturbations, which was confirmed by *Lilly*'s [1966] normal mode instability analysis. *Brown* [1980] investigated the impact of stratification on the inflection-point instability. He showed that the instability mode is damped by the stable stratification and cannot occur for Richardson number (R_i) > 0.25. For weak unstable stratification, $R_i > -0.04$, the instability is enhanced and the maximum growth rate shifts toward shorter wavelength and a more longitudinal orientation.

The convective instability or the so-called Rayleigh-Bènard instability is another major mechanism for generating ABL roll vortices. Linear normal mode analyses show that convective roll circulations orientate nearly
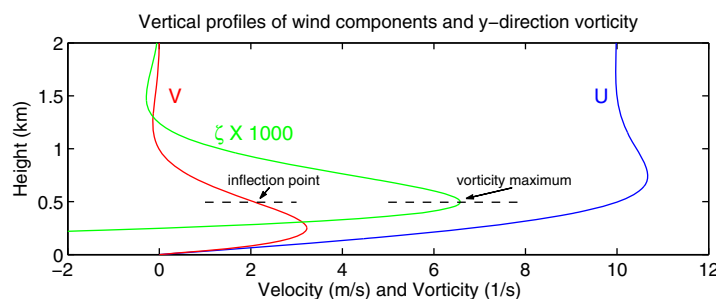
Figure 1. Vertical profiles of along-wind component (u), cross-wind component (v), and cross-wind direction vorticity (ς) of a classic Ekman-flow with a constant eddy viscosity in a coordinate in which x axis is aligned with the downwind direction of the mean wind.

parallel to the direction of the mean shear in a vertical shear flow and the convective instability mode, which has a larger growth rate than that of inflection-point instability mode, enhances with the increase of unstable stratification [e.g., *Asai*, 1970; *Etling*, 1971; *Asai and Nakasui*, 1973; *Kelly*, 1977], suggesting that the inflection-point instability will be overwhelmed once the con-

vective instability initiates. According to the previous studies [e.g., *Deardorff*, 1972; *Grossmann*, 1982; *Walter and Overland*, 1984, *Brűmmer*, 1985], the onset of roll vortices due to dynamic and convective instabilities may be empirically determined by a stability parameter, $\frac{z_i}{L}$, where L is the Monin-Obukhov length and z_i is the ABL height. For a strong unstable stratification of $\frac{z_i}{L} \leq -25$, the convection usually takes the form of three dimensional cellular cells. For a moderate unstable stratification of $\frac{z_i}{L} \geq -5$, convection is likely to be found in the form of streamwise roll vortices. Mixed types of organized convective structures are often found for the stratification of $-25 < \frac{z_i}{L} < -5$. For weak unstable stratification or near-neutral stratification of $\frac{z_i}{L} \geq -2$, convection is unlikely and the dynamic instability takes over. A thorough review on the formation and structure of ABL roll vortices can be found in *Etling and Brown* [1993].

Early in the 60s, *Faller* [1961] had already noted that the Ekman layer instability modes shown in theoretical studies may be responsible for the formation of spiral rainbands in tropical cyclones (TCs). Although it is now known that spiral rainbands have a much larger scale both in horizontal and vertical than that of ABL roll vortices [*Gall et al.*, 1998] and are generated by different mechanisms other than Ekman layer instabilities [e.g., *Chen and Yau*, 2001; *Wang*, 2002], the recent advances in remote sensing measurements, such as Doppler radar and Synthetic Aperture Radar (SAR), do reveal intense streamwise roll vortices and organized large eddy circulations at kilometer to sub-kilometer scales existing in the ABL of TCs (TCBL) [e.g., *Wurman and Winslow*, 1998; *Morrison et al.*, 2005; *Katsaros et al.*, 2000]. Motivated by the observed TCBL roll vortices, *Foster* [2005] made a local nonlinear instability analysis of the TCBL with a stratification determined by $\Delta T_v = T_v(z_s) - T_v(0)$ in a range from 0 to -5 K, where $T_v(0)$ and $T_v(z_s)$ are the virtual temperature at the surface and top of the surface layer, respectively. The orientation, scale, and strength of the circulations derived in *Foster*'s [2005] analysis agree well with the observed roll vortices in the TCBL. Using the first order K-closure and surface layer relations, the stability parameter may be rewritten as $\frac{z_i}{L} = -\frac{z_i g \Delta \bar{\theta}_v}{\theta_v (\Delta u)^2}$, then, the range of TCBL stratification considered by *Foster* [2005] is equivalent to $0 \geq \frac{z_i}{L} \geq -0.42$ if taking $z_i = 1000$ m, $\bar{\theta}_v{}^v = 300$ K, and $\Delta u = 20$ ms^{-1}. Although this is only a rough estimation, it suggests that the instability analyzed by *Foster* [2005] is basically the local Ekman layer dynamic instability in neutral or weak unstable stratifications according to the empirical criteria of roll instability onset summarized previously. It, thus, remains unclear if the observed TCBL roll vortices were generated by the convective instability or by dynamic instability. Nonetheless, *Foster*'s [2005] theoretical analyses indicate that roll vortices can be prevalent in the near neural or weak unstable TCBL.

A realistic simulation of three dimensional (3D) TCBL roll vortices is a challenge since the traditional approach of large eddy simulation (LES) cannot be simply applied to the TCBL. The double periodic lateral boundary conditions used by LES are no longer appropriate due to the movement of a TC vortex, horizontal inhomogeneity, and swirling winds that change their direction and speed continuously, which all tend to cause the condition at the inflow boundary to be different from that at the outflow boundary. Using a hindcasting LES nested in the mesoscale simulation of Weather & Research Forecasting (WRF) model [*Skamarock et al.*, 2008; *Zhu*, 2008a, 2008b] first explicitly simulated the TCBL roll vortices in a realistic environment during the landfall of Hurricane Ivan (2004) and Hurricane Katrina (2005). The structure of the simulated roll vortices including roll width, depth, and orientation is consistent with observations [*Wurman and Winslow*, 1998; *Morrison et al.*, 2005; *Katsaros et al.*, 2000]. In *Zhu*'s [2008a, 2008b] WRF-LES, the atmospheric model is coupled with a land-surface model. Thus, the TCBL stratification that determines the onset of dynamic and

convective instabilities is adequately predicted by the coupled system. In addition, since the land surface temperature during the hurricane landfall does not change much, the uncertainty of instability onset due to the error in estimating land surface temperature should be minimal.

Over the ocean, the storm induced upwelling due to Ekman pumping, vertical mixing in the upper ocean mixed layer, and evaporative heat loss to the atmosphere can lead to a substantial cooling of sea surface temperature (SST) underneath a TC. Observations show that the storm-induced SST cooling can be up to 3–7°C [e.g., *Bender et al.*, 1993; *Walker and Leben*, 2005]. *Sakaida et al.* [1998] even reported a maximum of 9°C SST cooling after the passage of a typhoon. Furthermore, the TC induced large ocean surface waves can affect the TC structure and intensity, especially the variability of surface winds [e.g., *Chen et al.*, 2013]. Leaving aside the issue of how the storm-induced SST cooling affects the TC intensification, such a strong cooling of SST should have a substantial impact on the stratification and structure of TCBL. Indeed, *Lee and Chen* [2012, 2014] showed interesting structural changes of TCBL caused by the storm-induced SST cooling in their fully coupled model simulations of Hurricane Frances (2004) and Typhoon Choi-Wan (2009). However, the TCBL roll vortices were not resolved in *Lee and Chen*'s [2012, 2014] simulations due to a coarse grid-spacing. There are several questions regarding the TCBL roll vortices that have never been tackled. First, will the error in estimating TCBL stratification due to the failure of considering the storm-induced SST cooling mistakenly initiate the onset of dynamic and convective instabilities of roll vortices? Second, are there significant differences in structure between the dynamically and convectively induced roll vortices? And finally, will the roll vortices generated by different instability mechanisms substantially affect the vertical transport in the TCBL? The answers to these questions not only can advance our understanding of air-sea interaction at the large turbulent eddy scale, which is currently poorly understood, but also is critical to a correct prediction of dispersion and advection of oil spill fumes at the ocean surface and aerial pollution transport in the ABL under extreme weather conditions. For example, the transport of oil slick from the Deepwater Horizon (DWH) oil spill occurred from 10 April to 15 July 2010, was greatly affected by the tropical storm Bonnie (2010) as it traveled across the Gulf of Mexico in late July 2010 [*Scalise*, 2013]. However, how roll vortices generated by dynamic and convective instability in TCBL affect the local mixing processes and long-range marine-to-land transport of oil slick is largely unknown.

In this study, we tackle the questions raised previously using the numerical experiments of Hurricane Isaac (2012) by WRF-LESs forced by the Unified Wave INterface-Coupled Model (UWIN-CM) [*Chen and Curcic*, 2015] that realistically simulates the SST cooling induced by TCs and forced by the NCEP FNL (Final) operational global analysis SST that does not include the storm-induced SST cooling. There are a few features associated with the storm-induced SST cooling that may affect TCBL roll vortices. These include magnitude, spatial distribution, and temporal variation of SST cooling. In this study, we investigate how the magnitude of SST cooling affects the TCBL roll vortices generated by the dynamic and convective instabilities. This manuscript is organized as follows. Section 2 describes the numerical experiment setup. The detailed analyses of simulations are presented in section 3. Conclusions and discussions will be given in section 4.

2. Numerical Experiment Setup

In this study, a WRF-LES configured from a multiply two-way nested WRF is used to explicitly simulate a spectrum of scales from large-scale background flow, TC vortex, mesoscale organizations, down to fine scale turbulent eddies in a unified system illustrated by Figure 2. The innermost domain of this multiply nested WRF has a resolution both in horizontal and vertical comparable to the typical grid-spacing used in LESs. WRF-LES distinguishes from the classic LES in that it enables the robust up-scale and down-scale interactions across a spectrum of scales, which is particularly important for the TCBL simulation since unlike the locally forced ABL the evolution of TCBL flow involves a complicated interplay among TC vortex, deep convection, mesovortices, and turbulent eddy circulations.

Hurricane Isaac (2012) is simulated in this study, which has a similar track in the Gulf of Mexico to Bonnie (2010) that had a great impact on DWH oil spill. Isaac became hurricane (category-1) at 12:00 UTC 28 August. As indicated in Figure 2, the locations when Isaac reached hurricane strength are close to the coast. Since this study focuses on the TCBL roll vortices over the ocean, the period of Isaac simulated in this study is from 21:00 UTC 27 to 12:00 UTC 28 August in total 15 h. The sustained wind speed during this period is 60 kt according to the best track data. This storm intensity is strong enough for the purpose of studying the
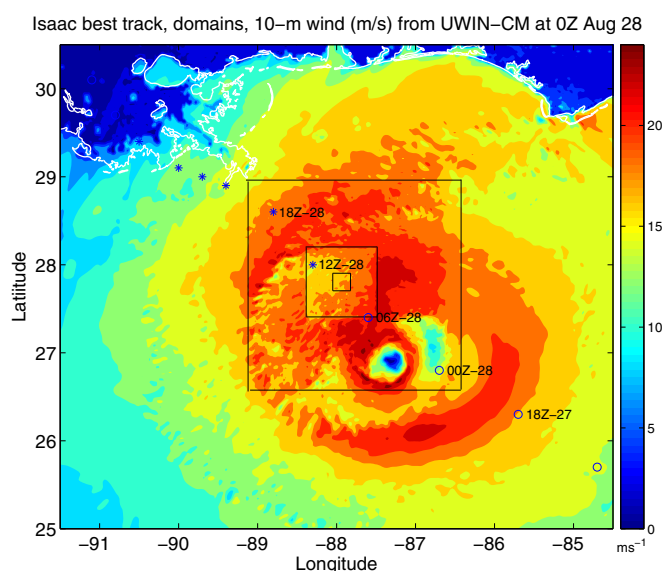
Figure 2. 10 m wind (color shades) at 0:00 UTC 28 August of Hurricane Isaac (2005) from the UWIN-CM simulation. Blue circles and stars are the best track of Isaac with stars indicating Isaac reaching hurricane intensity (>64 kt). Square boxes indicate the domains of WRF-LES.

TCBL roll vortices. The domain configuration of WRF-LES is set in a similar way to that of *Zhu* [2008a, 2008b]. As indicated in Figure 2, four fixed two-way nested domains with horizontal grid-meshes of 401X401 (D-1), 400X400 (D-2), 400X400 (D-3), and 301X301 (D-4) are configured. The grid spacing of the parent domain of WRF-LES (i.e., domain D-1) is set to 2 km. The nesting ratio of WRF-LES is set to 1:3 so that the grid-spacing of domains D-2, D-3, and D-4 is 666.67 m, 222.22 m, and 74.07 m, respectively. Domain D-1 is configured sufficiently large to cover most part of the Gulf of Mexico to allow for a realistic simulation of the large-scale flow. In order to obtain a better storm vortex structure, D-2 covers the inner core of Isaac during the entire 15 h simulation. The location of the innermost domain (D-4) is such chosen that it experiences most of the important events of the storm, such as outer rainbands, eyewall, and moat between rainband and eyewall, as Isaac moved toward the coast. All four domains have 71 levels in the vertical with a model top approximately at 21 km. Since this study focuses on the TCBL roll vortices, 40 levels are configured below 3 km with a grid-spacing stretching from 3.4 m in the surface layer to 113.4 m at 3 km.

WRF-LES is initialized and forced by the cloud resolving simulation of Isaac by UWIN-CM, which is a fully coupled atmosphere, surface wave, and ocean circulation modeling system. It consists of three components: (a) atmosphere model, WRF; (b) ocean wave model, the University of Miami Wave model (UMWW) [*Donelan et al.*, 2012]; (c) ocean circulation model, the HYbird Coordinate Ocean Model (HYCOM) [*Wallcraft et al.*, 2009]. The configuration of UWIN-CM is described in *Chen and Curcic* [2015]. UWIN-CM uses triple nests with a grid-spacing of 12 km, 4 km, and 1.3 km, respectively. In this study, the UWIN-CM data from the 4 km resolution grid are used to provide the initial, lateral boundary, and surface conditions for the parent domain (D-1) of WRF-LES. Since UWIN-CM only has 36 levels in the vertical, to appropriately initialize WRF-LES, the UWIN-CM data need to be interpolated onto the WRF-LES grid. This is done using WRF's one-way nesting feature to interpolate the 4 km grid UWIN-CM data at 21:00 UTC 27 August onto the D-1 gird of WRF-LES. As discussed in *Zhu et al.* [2010], a key to the success of WRF-LES is to gradually scale down from the synoptic scale flow to the large turbulent eddy scale to relax the discontinuity problem as the modeled atmosphere in the mesoscale domain, which is laminar by construction, flows into the turbulent LES domain. To allow for sufficient model spin-up, domains D-3 and D-4 are activated at 23:00 UTC 27 August, i.e., 2 h later after the start of integration of D-1 and D-2. To ensure the large-scale vortex flow in which the TCBL roll vortex is embedded simulated by WRF-LES does not drift away from that of UWIN-CM, the WRF-LES D-1 simulation is nudged toward the UWIN-CM 4 km grid simulation. Nudging is not activated in domains D-2, D-3, and D-4 to allow for a full development of TCBL roll vortices.

A key model physics of this multiple scale WRF simulation is the treatment of sub-grid scale (SGS) turbulent mixing. At the LES resolution, large turbulence eddies are explicitly resolved, and thus, only small-scale turbulence needs to be parameterized. Since smaller scale turbulent eddies are less flow-dependent and more isotropic, a three-dimensional (3-D) SGS turbulent mixing scheme is needed to parameterize 3-D isotropic small-scale eddies. In this study, the *Deardorff* [1970] 1.5-order closure turbulent kinetic energy (TKE) 3-D turbulent mixing scheme, which is commonly used to treat SGS mixing in classic LESs, is used for parameterizing SGS turbulent mixing in domains D-3 and D-4. For the coarser resolution domains, the isotropic
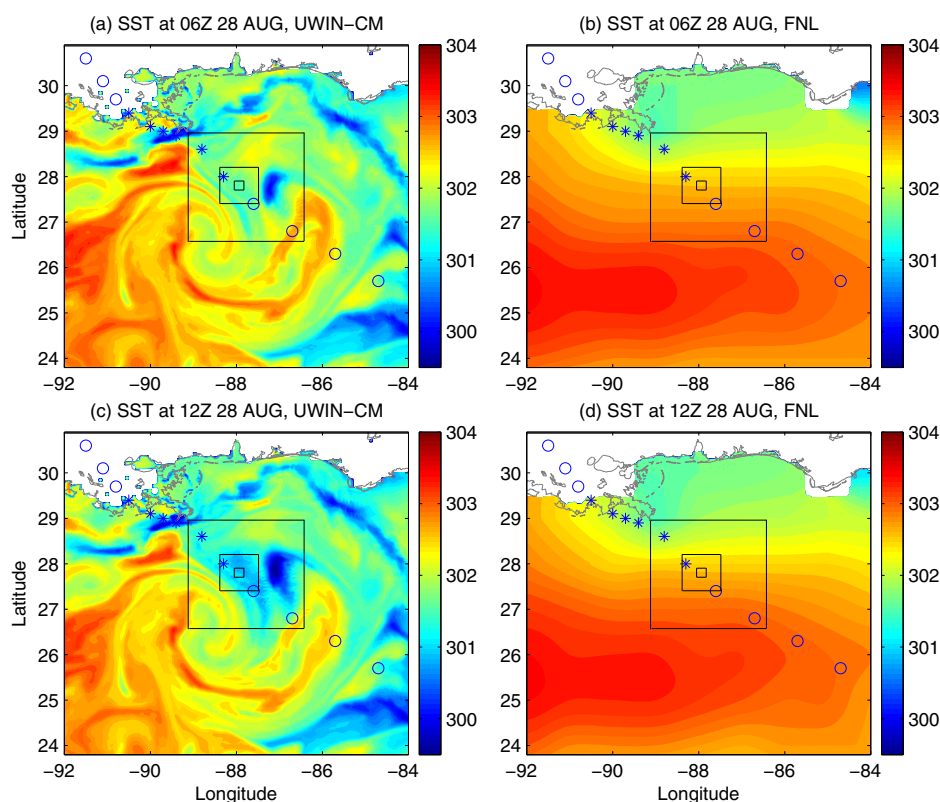
Figure 3. (a, c) SST at 06 UTC and 12 UTC from the UWIN-CM simulations. (b, d) SST at 06 UTC and 12 UTC from FNL analysis. Boxes, circles, and stars have the same meaning as those in Figure 2.

turbulence assumption is no longer valid. Therefore, the WRF one-dimensional (1-D) vertical turbulent mixing scheme, Yonsei University Scheme (YSU) [*Hong and Dudhia*, 2003] was activated in place of the 3-D TKE scheme to account for the vertical transport associated with the vertical SGS mixing processes in domains D-1 and D-2. Other major model physics include the Rapid Radiative Transfer Model (RRTM) [*Mlawer et al.*, 1997] and *Dudhia* [1989] scheme for longwave and shortwave radiation parameterization, respectively; and Thompson scheme [*Thompson et al.*, 2004, 2008] for cloud microphysics.

Two experiments are conducted in this study. In the first experiment, the SST in the four domains of WRF-LES is updated from the UWIN-CM simulation every hour during the integration of WRF-LES. This experiment is named as EXP-UWIN-CM hereafter. To investigate the impact of SST on the simulated TCBL roll vortices, the second experiment is designed exactly the same as the first experiment except that the SST is replaced by the mean SST between 18:00 UTC 27 and 00:00 UTC 28 August from the NCEP FNL (Final) Operational Global Analysis. Since the FNL SST does not change much from 18:00 UTC 27 to 12:00 UTC 28 August, the initial SST is kept the same during the entire simulation of the second experiment. This experiment is named as EXP-FNL hereafter. Figure 3 compares the SST at 06:00 UTC and 12:00 UTC 28 August simulated by UWIN-CM with the FNL SST. It clearly shows that there is a significant storm-induced SST cooling in the UWIN-CM simulation. It is, thus, interesting to see how this cooling of SST affects the structure of TCBL roll vortices and the circulation induced vertical transport in the TCBL. As shown in Figure 3, the storm-induced SST cooling has a substantial spatial variation at the TC vortex scale. However, due to the limitation of our computing ability the innermost domain D-4 of WRF-LES configured in this study can only cover an area of approximately 22 X 22 km^2 in which the spatial variation of SST is negligible. In addition, the SST is updated hourly from UWIN-CM. These two limitations in numerical setup make it impossible to explore the impact of spatial and temporal variations associated with the storm-induced SST cooling on TCBL roll vortices. But they should not affect the focus of this study on investigating how the error in SST estimation due to the failure of considering the storm-induced SST cooling might affect the generation of roll vortices by dynamic and convective instabilities and the impact of roll vortices generated by different mechanisms on the vertical transport in the TCBL.
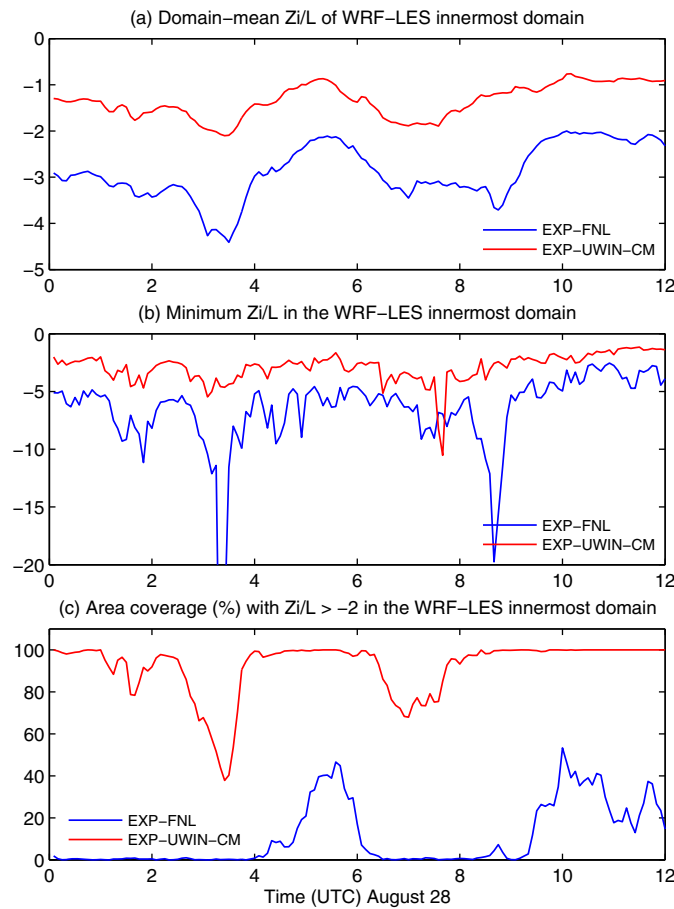
Figure 4. (a) Time series of mean stability parameter, $\frac{z_i}{L}$, averaged over the innermost domain (D-4) from EXP-UWIN-CM and EXP-FNL. (b) Time series of minimum stability parameter, $\frac{z_i}{L}$, in the innermost domain (D-4). (c) Time series of area coverage with $\frac{z_i}{L} > -2$ in the innermost domain (D-4).

3. Analysis Results

As summarized in the introduction, a key parameter that may be used empirically to determine the onset of ABL roll vortices is the stability parameter defined by $\frac{z_i}{L}$, where the Monin-Obukhov length is defined as $L = -\frac{\theta_0 u_*^3}{kg\overline{w'\theta'}_v}$, κ, g, θ_0, $u*$, and $\overline{w'\theta'}_v$ are the Von-Karman constant, gravitational acceleration, potential temperature at surface, friction velocity, and kinematic surface buoyancy flux, respectively. The surface buoyancy flux is calculated as $\overline{w'\theta'}_v = (1 + 0.608\bar{r})\overline{w'\theta'} + 0.608\bar{\theta}\overline{w'r'}$, where w, θ_v, r denote the vertical velocity, virtual potential temperature, and water vapor mixing ratio. Overbar and prime indicate mean and perturbation. $\overline{w'\theta'}$ and $\overline{w'r'}$ are the kinematic surface sensible and latent heat fluxes. Since friction velocity and surface sensible/latent heat flux are available in the standard WRF output, the Monin-Obukhov length L can be readily calculated from the model output. An appropriate definition of the ABL depth z_i is not scientifically trivial in the TC conditions. Unlike non-TC conditions in which the turbulent layer is normally cleanly separated from the free atmosphere above by a well-defined

inversion, it is often difficult to distinguish the turbulence directly affected by the surface processes from that associated with convective clouds in TC conditions since there is no clean physical interface (or discontinuity), such as a strong inversion, that separates the TCBL from the free atmosphere above. Two methods can be found in literature to define the depth of TCBL. One is the thermodynamic mixed layer defined based on the conservative thermodynamic variables, such as liquid water potential temperature θ_l and total water mixing ratio q_t. This method is often difficult to apply in TC conditions due to the lack of a clean discontinuity in the vertical profiles, particularly in the eyewall and rainbands. The second is the dynamic radial inflow layer defined by the height where radial inflow turns to radial outflow. The TC surface inflow layer can be accurately determined from the simulated wind fields. Since the dynamic instability is a prevalent mode for generating roll vortices in the TCBL [*Foster*, 2005], it is natural to use the dynamically defined TCBL depth to estimate the stability parameter. Figure 4 compares the statistics of $\frac{z_i}{L}$ over the innermost domain (D-4) between the two experiments, EXP-UWIN-CM and EXP-FNL. The failure of considering the storm-induced SST cooling by the FNL SST significantly overestimates the TCBL instability. The domain-mean $\frac{z_i}{L}$ in EXP-UWIN-CM is consistently greater than -2, satisfying the dynamic instability onset of rolls according to the empirical criterion obtained in the non-TC conditions summarized in the introduction. In contrast, the domain-mean $\frac{z_i}{L}$ in EXP-FNL falls in the range for the onset of roll vortices by the convective instability. Although there exist mixed types of instability modes for roll generation in both experiments, the area coverage of $\frac{z_i}{L} > -2$ shown in Figure 4c suggests that the dynamic instability is a dominant mode in EXP-UWIN-CM in contrast to EXP-FNL in which the convective instability mode dominates. There are substantial temporal fluctuations in the calculated stability in both experiments. Such a temporal variation of stability likely results from the combined effect of the SST change associated with the warmer filament or cold wake of SST in the coupled model as the storm passes
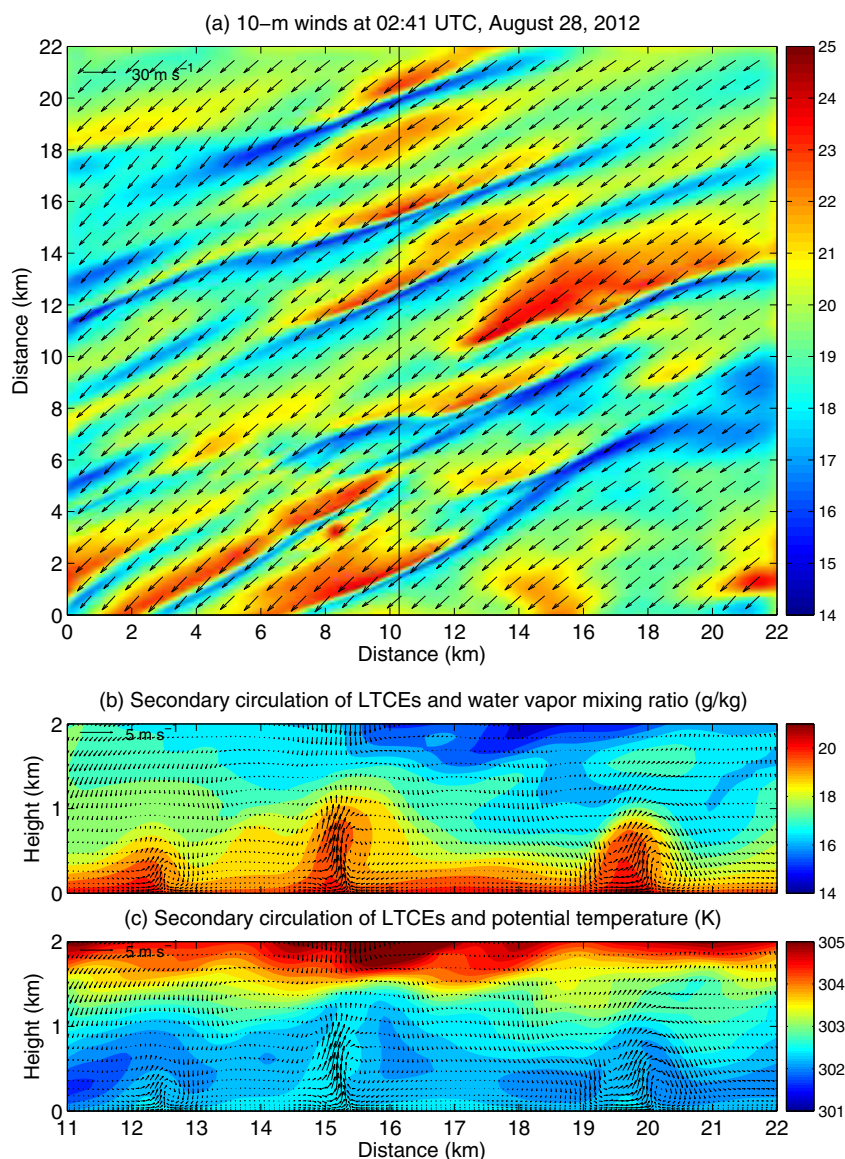
Figure 5. (a) Simulated 10 m wind speed (color shades) and wind vectors at 2:41 UTC in the innermost domain (D-4) from EXP-UWIN-CM. Black line indicates the location of cross-section shown in Figures 5b and 5c. (b, c) Vertical cross-section water vapor mixing ratio and potential temperature (color shades) and overturning roll circulations (arrows). To better illustrate the vertical overturning circulations, the mean horizontal wind has been removed.

over the innermost domain of D-4 and the nonlinear interaction between ocean surface and the ABL above it as documented in *Lee and Chen* [2012, 2014]. The results shown in Figure 4 suggest that failure of considering the storm-induced SST cooling may completely remove the dynamic instability from the TCBL, which would otherwise occur over a cooler ocean surface induced by a storm. It, however, should be kept in mind that there are uncertainties in this estimation. First, the way of calculating z_i could affect the value of stability parameter. It raises a question how to appropriately extend this empirical criterion of roll onset to TC conditions. Second, although, to the first-order approximation, the main processes that govern ABL turbulence should be the same irrespective of weather conditions, the unique dynamic and thermodynamic structure of a TC could yield a different critical stability that separates the onset of dynamic and convective instabilities. Further research is needed to clarify these issues. Nonetheless, it warns that inappropriate SST prescribed in numerical simulations may substantially change the onset of instability modes for roll generation when model resolution becomes high enough for resolving large turbulent eddy circulations.
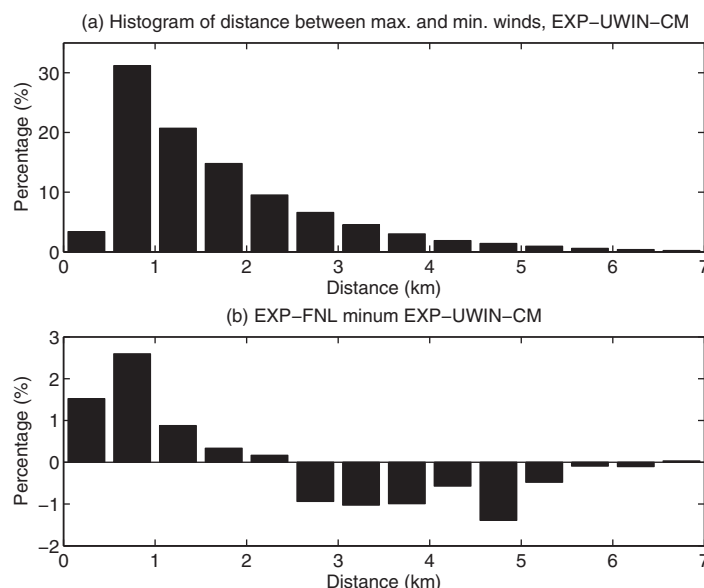
Figure 6. (a) Histograms of the distance between the cores of maximum and minimum winds in the surface wind bands from 0:00 UTC to 12:00 UTC 28 August from EXP-UWIN-CM. (b) Difference between EXP-FNL and EXP-UWIN-CM, i.e., values of EXP-FNL minus values of EXP-UWIN-CM.

The high resolution data from the innermost domain (D-4) can be used to examine the dynamic and thermodynamic structure of TCBL roll vortices. Figure 5 shows a snapshot of the simulated 10 m wind fields at 02:41 UTC 28 August from EXP-UWIN-CM. The horizontal surface wind speed exhibits the well-organized structures consisting of pairs of streamwise maximum and minimum wind bands aligning at a slight angle to the wind direction. These aligned wind band structures are similar to the radar observed roll vortices in Hurricanes Fran (1996), Bonnie (1998), and Georges (1998) reported by *Morrison et al.* [2005]. The orientation of streamwise wind bands with respect to the wind direction is consistent with the theoretical analysis of dynamic instability induced roll circulations. Comparing the horizontal plane view of wind bands (Figure 5a) with the vertical overturning circulation shown in the vertical cross-section plot (Figures 5b and 5c), it is clear that the maximum winds are associated with the downward leg of rolls and the minimum winds correspond to the upward motion. This is consistent with the typical structure of TCBL roll vortices derived from observations [e.g., *Wurman and Winslow*, 1998] that the downward leg of the circulation transports momentum aloft to the surface resulting in local surface wind maximum, while the upward leg normally corresponds to the momentum minimum, reflecting air slowed down by the surface friction. The unevenly distributed vertical velocities shown in the overturning circulations, i.e., narrow strong updrafts compensated by broad weak downdrafts, suggest that the vertical velocity associated with TCBL roll vortices is positively skewed. The magnitude of the vertical velocity shown in Figures 5b and 5c is very close to that estimated from the radar observations [*Morrison et al.*, 2005]. As indicated by Figure 5b, the updraft of the circulations tends to transport moist surface air upward and the downdraft entrains dry air aloft downward. In such a way, the TCBL roll vortices directly connect the surface, the TCBL, and the main body of a TC to enhance the exchange of energy, moisture, and momentum between them, and thus, they should play a critical role in the development of a TC. Although water vapor mixing ratio is not a conservative scalar, what is shown in Figure 5b should provide a first-order depiction of aerial pollutant transport by large turbulent eddies in the TCBL.

From Figure 5, one may infer the width of TCBL roll vortices although an accurate determination of roll width is not easy. As the figure illustrated, the distance between the maximum and minimum winds may be considered as a good proxy for half of the roll width. Using this definition, a statistical estimate of roll width is done from 0:00 UTC to 12:00 UTC for both simulations (Figure 6). The distance between maximum and minimum wind speed associated with TCBL roll vortices (i.e., half of the roll width) peaks at approximately 500–1000 m. The range of roll vortices brackets the roll width derived from the WSR-98D radar observations [*Morrison et al.*, 2005], although the definition of roll width used here is different from that of *Morrison et al.* [2005]. The statistics also show that the failure of considering the storm-induced SST cooling only causes a slight increase in roll vortices with smaller roll widths but reduces the roll vortices with larger roll widths. The T-test shows that the difference shown in Figure 6 is statistically significant at the 0.05 level, which is further confirmed by the Kolmogorov-Smirnov test. However, a statistically significant difference may not be important. As shown in Figure 6b, the difference in roll width is less than 3%. At the first glance, it seems to be a surprise that the roll vortices generated by the dynamic and convective instability only have a marginal difference in their width considering that the two instability modes have completely different triggering mechanisms. A possible reason is that the TCBL rolls are constrained by the depth of the
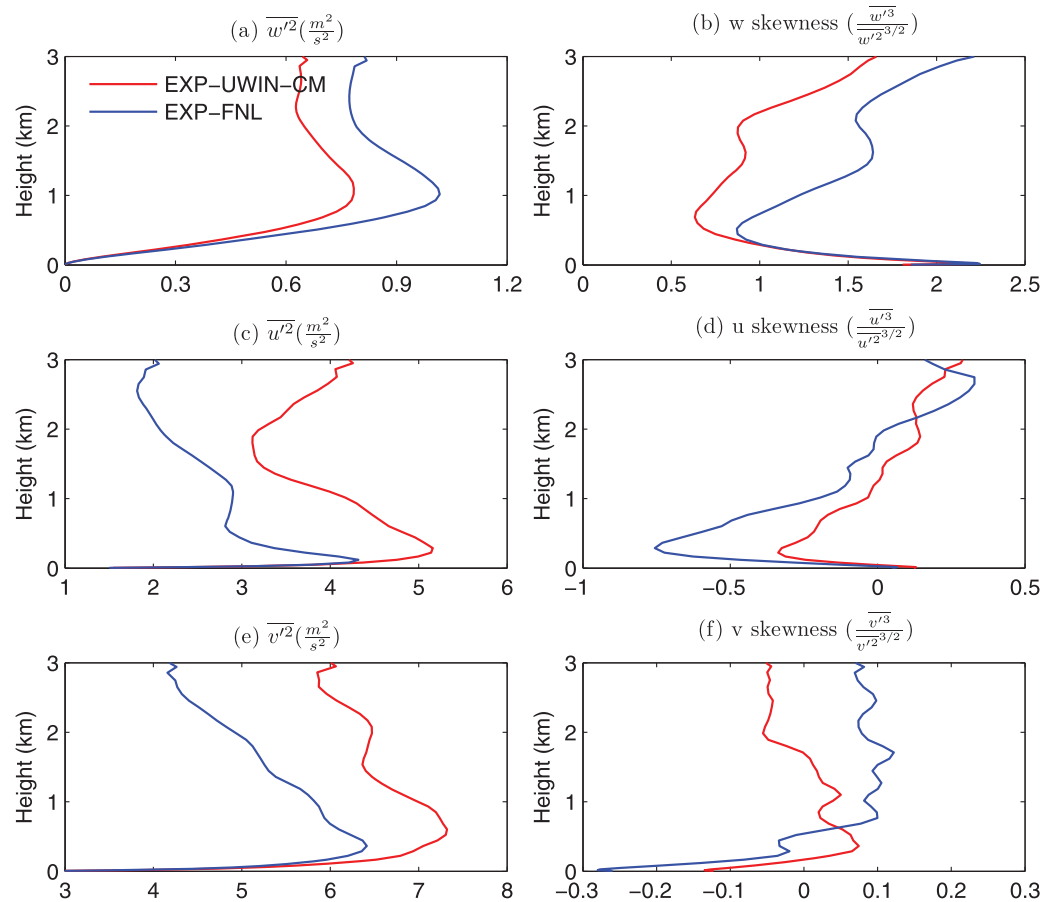
Figure 7. (a, c, e) Variance of vertical velocity, x direction wind component, and y direction wind component of the innermost domain (D-4) in a coordinate in which x axis is aligned with the domain-mean wind vector during the time period from 2:30 UTC to 4:00 UTC 28 August. (b, d, e) Skewness of vertical velocity, x direction wind component, and y direction wind component of the innermost domain (D-4).

TCBL although its definition is still a matter of debate. Such a strong constraint on the roll vortices by the depth of TCBL should have an impact of the roll width. To further clarify this issue, theoretical analysis is needed to understand the factors governing the width of roll circulations generated by dynamic and convective instability modes.

To further understand the difference of TCBL eddy structure due to the change in TCBL stability caused by the storm-induced SST cooling, we calculated some statistics of model resolved wind components in the innermost domain (D-4). As an illustration, Figure 7 compares the variance and skewness of the resolved vertical velocity and horizontal wind components from 2:30 to 4:00 UTC 28 August between the two experiments, where horizontal wind components, u and v, represent the along-wind and cross-wind components in a coordinate in which x axis is aligned with the domain-mean wind vector. As shown in Figure 4, this is a period in which the two simulations have the largest difference in TCBL stability. The comparison shows that EXP-UWIN-CM generates a larger horizontal velocity variance but smaller vertical velocity variance than EXP-FNL. This result is somewhat expected since convective and dynamic instability should generate anisotropic eddy circulations. While strong convective instability can lead to large perturbations in vertical velocity, the large wind shear associated with strong dynamic instability should result in large variances in horizontal wind components. Since the sum of velocity variances represents TKE, this result indicates that the storm-induced SST cooling can lead to a larger TKE due to the dynamic instability despite that the SST cooling stabilizes the TCBL.

The skewness clearly shows that the TCBL eddy circulations are highly skewed in the vertical velocity consistent with what is shown in Figure 5 that the narrow strong updrafts are compensated by the broad weak downdrafts. But both along-wind and cross-wind components are nearly normally distributed. The impact
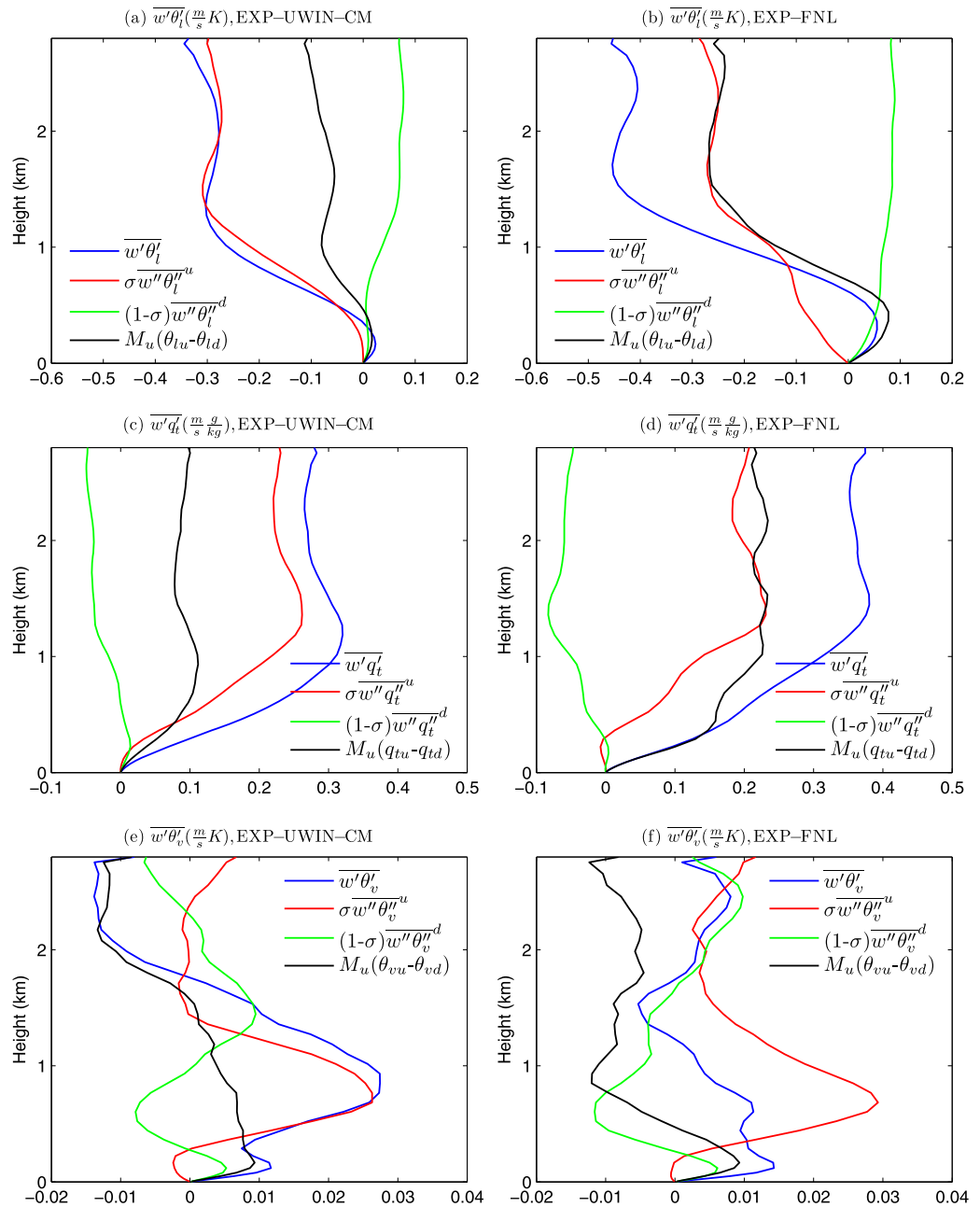
Figure 8. Vertical profiles of model resolved fluxes, $\overline{w'\theta_l'}$, $\overline{w'q_t'}$, and $\overline{w'\theta_v'}$ in the innermost domain (D-4) averaged over the period from 2:30 UTC to 4:00 UTC, and the decomposed components based on the mass-flux top-hat profile (i.e., equation (1)) from EXP-UWIN-CM and EXP-FNL.

of TCBL stability on eddy circulations is apparent. The stronger TCBL convective instability causes more skewed eddy circulations with an interesting feature that the relatively small skewness of horizontal winds is mainly concentrated in the low levels and the large skewness of vertical velocity increases with height.

Figure 8 shows the domain-mean vertical profiles of model resolved vertical fluxes of conservative thermodynamic variables, θ_l and q_t, and buoyancy fluxes averaged over the same time period (2:30–4:00 UTC) as that of Figure 7. It shows that the increased convective instability in EXP-FNL enhances the vertical transport of thermodynamic variables. Note that the TKE in this period is larger in EXP-UWIN-CM than in EXP-FNL. It suggests that although turbulent intensity and turbulent transport are related, the stronger turbulent intensity (measured by TKE) resulting from the dynamic instability does not necessarily ensure the larger vertical

transport of heat and moisture (An explanation will be provided shortly). As shown in Figure 5, the organized TCBL roll vortices consist of well-defined updrafts and downdrafts. It is these coherent structures that are responsible for the efficient nonlocal vertical transport.

To better understand the difference in vertical transport induced by the roll vortices generated by the convective and dynamic instabilities in EXP-UWIN-CM and EXP-FNL, we first decomposed the model resolved vertical fluxes based on a top-hat profile commonly used for estimating the coherent feature induced vertical transport in moist convection [*Arakawa and Schubert*, 1974]. In this framework, the total kinematic vertical flux of a generic variable χ at an arbitrary height may be decomposed into three parts,

$$\overline{w'\chi'} = \sigma\overline{w''\chi''}^c + (1-\sigma)\overline{w''\chi''}^e + M_c(\bar{\chi}^c - \bar{\chi}^e), \tag{1}$$

where $M_c = \sigma(1-\sigma)(\bar{w}^c - \bar{w}^e)$ is known as the kinematic convective mass flux, σ is the fraction of coherent elements of an area. Overbar and overbar indexed with superscripts c and e indicate the averages over the area, the coherent convective elements, and the environment in which the coherent elements are embedded, respectively. Prime and double prime indicate the perturbations with respect to the domain-mean and mean over the coherent convective elements and environment, respectively. To obtain equation (1), the top-hat distribution profile has been applied to the mean fields, i.e., $\bar{\chi} = \sigma\bar{\chi}^c + (1-\sigma)\bar{\chi}^e$. The first and second terms on the right-hand side (RHS) of equation (1) represent the fluxes induced by the perturbations within the coherent elements and environment, respectively. The third term on the RHS of equation (1) represents the fluxes induced by the coherent features. Using this method, we decomposed the resolved vertical fluxes of θ_l and q_t, and buoyancy fluxes based on the coherent features defined by updraft ($w > 0.01$ ms^{-1}). The corresponding decomposed vertical profiles of fluxes are provided in Figure 8. In EXP-FNL, the mean up-downdraft contributes a significant proportion to the total flux $\overline{w'\theta'_l}$ and $\overline{w'q'_t}$ (Figures 8b and 8d). Considering the strong convective instability in EXP-FNL, this result seems to be consistent with the mass-flux dynamic view of convection that the coherent structures consisting of strong updrafts and the associated downdrafts are mainly responsible for the vertical transport of conservative thermodynamic variables. In contrast, in EXP-UWIN-CM, the mean up-downdraft only contributes a small proportion to the total flux $\overline{w'\theta'_l}$ and $\overline{w'q'_t}$ (Figures 8a and 8c). Most of the fluxes are contributed by the perturbations inside the mean updraft. This result is interesting but may be understood from the fundamental difference in the roll circulations generated by the convective and dynamic instabilities. Physically, the updrafts of convectively driven circulations should be related to thermal plumes or cells originated at the surface that possess similar thermodynamic properties. During the adiabatic rising, the convective updrafts conserve their reversible thermodynamic properties, such as θ_l and q_t, to a good approximation, implying that θ_l and q_t should have a good correlation with the convective updraft to result in a large $\overline{w'\theta'_l}$ and $\overline{w'q'_t}$. On the other hand, the updrafts of dynamically driven circulations do not necessarily have similar conservative thermodynamic properties, which reduces the correlation between the mean updraft and mean conservative thermodynamic properties leading to a small contribution to the total $\overline{w'\theta'_l}$ and $\overline{w'q'_t}$. The decomposition of buoyancy flux shows different but interesting features. In EXP-UWIN-CM, similar to the decomposition of vertical fluxes of conservative thermodynamic variables, the perturbations inside the updraft also contribute significantly to the total resolved buoyancy fluxes. However in EXP-FNL, the coherent mean up-downdraft is no longer a main contributor to the total resolved buoyancy fluxes. This change may be due to the fact that θ_v is not a reversible thermodynamic variable, which causes the behavior of vertical buoyancy flux to be different from that of vertical fluxes of conservative thermodynamic variables.

Although the mass-flux decomposition of fluxes provides a means to reveal the difference in vertical transport induced by convectively and dynamically driven TCBL roll circulations, the top-hat profile used for decomposition oversimplifies the rich scales of turbulent eddies in the TCBL. To better understand the transport processes in terms of scales, the resolved fluxes and variances by the innermost domain (D-4) of WRF-LES are decomposed by the two-dimensional fast Fourier transform (2D-FFT) in terms of wavenumbers. A detailed description of 2D-FFT is provided in the Appendix A. To illustrate the impact of the storm-induced SST cooling on TCBL eddy structure and vertical transport, Figure 9 show the power spectra of vertical velocity and cospectra and phase spectra of $\overline{w'\theta'_v}$ as function of total wavenumber index averaged below 3 km and over the same time period (2:30 – 4:00 UTC) as that in Figures 7 and 8. The peak w spectra occurs approximately at 10 wavenumber. Since the length of the innermost domain (D-4) is $74.07 \times 300 = 22,221$ m, the peak wavenumber 10 corresponds to a spatial scale of approximately 2,221 m.
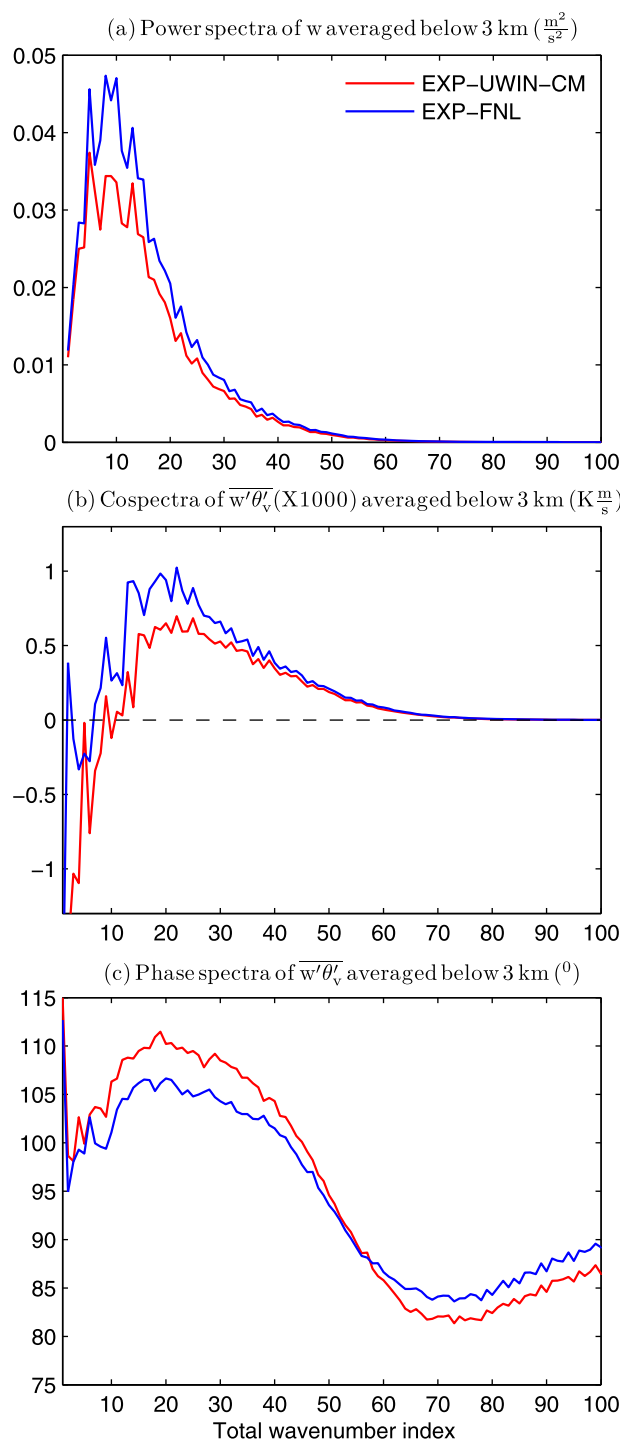
Figure 9. (a) Power spectra of vertical velocity; (b) Cospectra of $\overline{w'\theta'}_v$; and (c) Phase spectra of $\overline{w'\theta'}_v$ averaged below 3 km over the period from 2:30 UTC to 4:00 UTC from EXP-UWIN-CM and EXP-FNL.

This is consistent with the classic view of turbulent energy cascade that the large eddies are the energy-containing eddies. The scale of peak power spectra, however, appears to be larger than that obtained in non-TC conditions [e.g., *Kaimal et al.*, 1972, 1976; *Busch*, 1973], indicating that the strong TC-force wind causes the energy-containing eddies to shift toward the larger scales. The increased convective instability in EXP-FNL enhances the magnitude of w power spectra, but it does not appear to change the scale of energy-containing eddies. Compared with power spectra of vertical velocity, the cospectra of buoyancy flux $\overline{w'\theta'}_v$ show interesting features. The most significant difference is that the scale of peak cospectra is shifted to a high wavenumber approximately 20, which corresponds to a spatial scale roughly 1,111 m, indicating that large energy-containing eddies are, in fact, the inefficient carriers of heat and moisture. The most efficient heat/moisture carrying eddies have scales smaller than that of large energy-containing eddies. This result has an important implication in numerical prediction of TCs. From the perspective of turbulent power spectrum only, the model grid-spacing (1 – 2 km) used in current cloud resolving mesoscale models seems to be sufficient to resolve most of turbulent energy of TCs. However, as shown in Figure 9b, there are still significant fluxes induced by turbulent eddies with wavenumber 30 (approximately 740 m in spatial scale), suggesting that to successfully account for the most important vertical transport processes a smaller model grid-spacing than 1 km in TC simulations is needed. Figure 9b also indicates that the enhanced TCBL convective instability only shifts the scale of peak cospectra of $\overline{w'\theta'}_v$ slightly to lower wavenumbers, and thus, the storm-induced SST cooling is not a key factor that can substantially affect the scales of eddies in carrying heat and moisture. As indicated by Figure 9c, the storm-induced SST cooling has a negligible effect on the phase spectra of $\overline{w'\theta'}_v$. Ideally, two variables 180° out of phase, 90° out of phase, and 0° in phase will yield maximum negative, zero, and maximum positive covariance respectively. The change in phase spectra of $\overline{w'\theta'}_v$ shown in Figure 9c suggests that part of the change in magnitude of cospectra $\overline{w'\theta'}_v$ shown in Figure 9b should be caused by the change in phase relationship between w and θ_v.

4. Conclusion and Discussion

Although the impact of storm-induced SST cooling on TC intensification has long been recognized and has been one of the research focuses of recent observational and numerical studies of TCs, to authors' knowledge, no study so far has ever studied how the storm-induced SST cooling affects the structure of the TCBL roll vortices generated by the convective and dynamic instability and the roll circulation induced vertical transport in the TCBL. This question is investigated in this study using two WRF-LES experiments of Hurricane Isaac (2012) forced by the mesoscale simulation of UWIN-CM, a fully coupled atmosphere-wave-ocean modeling system. In one experiment, which is named as EXP-UWIN-CM, the SST in WRF-LES is updated hourly from the UWIN-CM's simulation, whereas in the second experiment (named as EXP-FNL) the SST is replaced with FNL analysis that excludes the storm-induced SST cooling. The simulations show that the roll vortices are prevalent in the TCBL and the storm-induced SST cooling has a profound impact on the onset and structure of TCBL roll vortices and the vertical turbulent transport in the TCBL. The main results of this study are summarized as follows.

1. The mean TCBL stability parameter, $\frac{z_i}{L}$, in EXP-UWIN-CM is consistently greater than -2 satisfying the empirical criterion for dynamic instability onset of roll circulations, whereas the mean $\frac{z_i}{L}$ in EXP-FNL varies in the range from -5 to -2, suggesting that the roll vortices are generated by convective instability or mixed mode of convective and dynamic instability. Leaving aside the question whether the empirical criteria obtained in non-TC conditions can be extended to the TCBL and the uncertainties in the estimation of $\frac{z_i}{L}$, this result warns that failure to consider the storm-induced SST cooling could incorrectly initiate TCBL roll generation mechanisms. Although TCBL roll generation is only a SGS process in current mesoscale cloud resolving simulations of TCs, it could pose a serious problem when model grid resolution becomes sufficiently high that the TCBL roll vortices can be explicitly resolved in simulations. Without an appropriately responding ocean, the expected improvement of TC intensity forecast by further decreasing model grid-spacing to eddy resolving resolution might not be obtained due to the incorrectly generated TCBL roll vortices. From the material transport perspective, the TCBL roll vortices result in substantial variations of surface winds, such as the wind bands shown in Figure 5a, which not only may induce the SST change at large eddy scales to complicate the local air-sea interaction but also will exert a strong impact on the mixing in the oceanic mixed layer to affect substance mixing and dispersion at the ocean surface. This study provides a justification of the importance of TCBL roll vortices to the local advection and transport of oil spill fumes, such as those resulted from DWH oil slick. However, the detailed impact of TCBL roll vortices on the material transport at the ocean surface remains largely unknown and further research on this issue is needed.

2. The TCBL roll vortices generated by the convective and dynamic instability are anisotropic. While the former are more vertically oriented, the latter are more horizontally oriented. This is reflected by the larger vertical velocity variance in EXP-FNL that has a stronger convective instability, and larger variance of horizontal winds in EXP-UWIN-CM that is dominated by dynamic instability. The anisotropic TCBL roll vortices are also evidenced from the large skewness in vertical velocity. Increase of convective instability enhances the skewed structure of TCBL roll vortices.

3. Large convective instability in EXP-FNL induces large vertical fluxes of conservative thermodynamic variables, θ_l and q_t, and buoyancy fluxes; whereas the dominant dynamic instability in EXP-UWIN-CM leads to large TKE but relatively weak vertical transport of heat and moisture compared with EXP-FNL. This result suggests that strong turbulent intensity does not necessarily result in strong vertical transport and vice versa due to the different characteristics in roll vortices generated by convective and dynamic instability. For convectively driven circulations, the convective updraft often possesses similar thermodynamic properties, leading a good correlation between θ_l and q_t and convective updraft to result in a large $\overline{w'\theta'_l}$ and $\overline{w'q'_t}$. In contrast, the updraft of a dynamically driven circulation does not necessarily have similar conservative thermodynamic properties, which reduces the correlation between the updraft and conservative thermodynamic properties leading to a small contribution to the total $\overline{w'\theta'_l}$ and $\overline{w'q'_t}$. However, it remains uncertain if the above described features of vertical fluxes of thermodynamic variables also apply to the vertical material transport in the TCBL. This will be investigated in our future study.

4. The spectral and cospectral analyses show that the scale at which w power spectrum reaches the peak is, in fact, much larger than the scale of peak cospectrum of $\overline{w'\theta'_v}$, indicating that energy-containing eddies are not the most efficient in carrying heat and moisture. The comparison between EXP-UWIN-CM and

EXP-FNL shows that the change in convective and dynamic instability does not have an apparent effect on the scales of peak power spectrum and cospectrum. The implication is that numerical simulations with a grid resolution that can explicitly resolve the large energy-containing eddies may not successfully capture the important transport processes occurring at smaller scales, which, according to this study, are smaller than 1 km.

Two issues remain to be addressed. First, due to the limitation of computing resource, the LES domain configured in this study only covers a very small part of a TC vortex. Thus, it is impossible to tackle how the spatial variation of storm-induced SST cooling, which is substantial according to the UWIN-CM simulations, affects the TCBL roll vortices. Note that the spatial variation of SST simulated by UWIN-CM can affect winds in the outer domains of WRF-LES, which could pose an impact on the resolved TCBL roll vortices in the innermost domain, D-4. But this possible effect is not considered in our analyses. Second, in this study the storm-induced SST cooling is included in the simulation of WRF-LES through hourly SST updating during the model integration. Although the TCBL atmospheric flow shows a substantial response to the SST cooling induced by the storm, the ocean response to the change in atmospheric turbulent eddy circulations is absent in this one-way forcing experiment. As shown in this study, the TCBL tends to produce the roll vortices at scales of $O(10^2 - 10^3$ m) generated by the dynamic and convective instability in the TCBL. These streamwise roll vortices create substantially different surface winds (Figure 5) associated with the upward and downward branches of circulations. The significantly inhomogeneous surface winds at the large turbulent eddy scales should cause corresponding ocean responses leading to inhomogeneous SST change at the same roll scales, which can further cause the change in the local atmospheric stability to affect the energy and momentum exchange at the air-sea interface. Currently, the details of air-sea interaction at large eddy scales are mostly unknown. But understanding this important feedback between ocean and atmosphere and including it in numerical simulations are critical not only to a correct prediction of TC intensification but also to an appropriate simulation of oil spill advection and dispersion at the ocean surface and aerial pollution transport pathways in the TCBL. Exploring these questions will be the focus of our future research.

Appendix A: 2D-FFT

Let $w(m,n)$ and $\chi(m,n)$ be the vertical velocity and a generic scalar on a 2D model grid at an arbitrary height, where $m=0,1,\ldots,M-1$; $n=0,1,\ldots N-1$ are the model grid number index; and M and N are the number of model grids in x and y direction (for this study, $M=N=300$ for the innermost domain of WRF-LES), the 2D-FFT of $w(m,n)$ and $\chi(m,n)$, then, may be written as,

$$\hat{w}(k,l) = \frac{1}{NM} \sum_{m=0}^{M-1} \sum_{n=0}^{N-1} w(m,n) e^{-i(\omega_k m + \omega_l n)}, \tag{A1}$$

$$\hat{\chi}(k,l) = \frac{1}{NM} \sum_{m=0}^{M-1} \sum_{n=0}^{N-1} \chi(m,n) e^{-i(\omega_k m + \omega_l n)}, \tag{A2}$$

where k and l are the 2D-FFT wavenumber index in x and y direction, and $\omega_k = 2\pi \frac{k}{M}$, $k=[-\frac{M}{2}:1:\frac{M}{2}-1]$; $\omega_l = 2\pi \frac{l}{N}$, $l=[-\frac{N}{2}:1:\frac{N}{2}-1]$. $\frac{\omega_k}{\Delta x}$ and $\frac{\omega_l}{\Delta y}$ are the angular wavenumber in x and y direction respectively. In this study, $\Delta x = \Delta y = 74.07$ m. The spectral energy, then, may be written as

$$E_w(k,l) = \hat{w}(k,l)^* \cdot \hat{w}(k,j) = |\hat{w}(k,l)|^2; \quad E_\chi(k,l) = \hat{\chi}(k,l)^* \cdot \hat{\chi}(k,j) = |\hat{\chi}(k,l)|^2, \tag{A3}$$

where superscript * denotes the complex conjugate. One may also define the cross spectrum between $w(m,n)$ and $\chi(m,n)$ as,

$$G_{w\chi}(k,l) = \hat{w}(k,l)^* \cdot \hat{\chi}(k,j) = [\hat{w}(k,l)_r - i\hat{w}(k,l)_i][\hat{\chi}(k,l)_r + i\hat{\chi}(k,l)_i]$$

$$= [\hat{w}(k,l)_r \cdot \hat{\chi}(k,l)_r + \hat{w}(k,l)_i \cdot \hat{\chi}(k,l)_i] - i[\hat{w}(k,l)_i \cdot \hat{\chi}(k,l)_r - \hat{w}(k,l)_r \cdot \hat{\chi}(k,l)_i] \tag{A4}$$

$$= C_{w\chi}(k,l) - i Q_{w\chi}(k,l),$$

where subscripts r and i indicate the real and imaginary parts of a complex. $C_{w\chi}(k,l)$ and $Q_{w\chi}(k,l)$ are known as the cospectrum and quadrature spectrum, respectively. The Parseval's theorem states that the

sum of spectral energy and cospectral amplitudes over all 2D-FFT harmonics equals the variance of $w(m,n)$ and $\chi(m,n)$ and the covariance between them, respectively, i.e.,

$$\sum_{k=0}^{M-1}\sum_{l=0}^{N-1} E_w(k,l) = \overline{w'^2}; \quad \sum_{k=0}^{M-1}\sum_{l=0}^{N-1} E_\chi(k,l) = \overline{\chi'^2}; \quad \sum_{k=0}^{M-1}\sum_{l=0}^{N-1} C_{w\chi}(k,l) = \overline{w'\chi'}. \tag{A5}$$

While $C_{w\chi}(k,l)$ provides a way to decompose a vertical flux in terms of 2D-FFT harmonics, the quadrature spectrum, $Q_{w\chi}(k,l)$, describes the phase relationship between the two variables. The phase spectrum, then, may be defined as,

$$\Phi_{w\chi}(k,l) = 180^0 - \tan^{-1}\left(\frac{Q_{w\chi}(k,l)}{C_{w\chi}(k,l)}\right), \tag{A6}$$

$\Phi_{w\chi}(k,l)$ can be interpreted as the phase difference between $w(m,n)$ and $\chi(m,n)$ that yield the greatest correlation for any wavenumber index, k and l. $E_w(k,l)$, $E_\chi(k,l)$, $C_{w\chi}(k,l)$ and $\Phi_{w\chi}(k,l)$ are the spectra on a 2D-plane ($k = [-\frac{M}{2}:1:\frac{M}{2}-1]$; $l = [-\frac{N}{2}:1:\frac{N}{2}-1]$) centered at wavenumber zero. To better display the result of spectral analyses, defining a total wavenumber index, $K = \sqrt{k^2+l^2}$, then, the obtained spectra in a Cartesian coordinate $[k, l]$ may be rewritten in a polar coordinate $[K, \varphi]$. This allows one to define azimuthally integrated spectral energy and cospectrum, i.e., $\tilde{E}_w(K) = \sum_{\phi=0}^{2\pi} E_w(K,\phi)$, $\tilde{E}_\chi(K) = \sum_{\phi=0}^{2\pi} E_\chi(K,\phi)$, $\tilde{C}_{w\chi}(K) = \sum_{\phi=0}^{2\pi} C_{w\chi}(K,\phi)$, satisfying $\sum_K \tilde{E}_w(K) = \overline{w'^2}$, $\sum_K \tilde{E}_\chi(K) = \overline{\chi'^2}$, $\sum_K \tilde{C}_{w\chi}(K) = \overline{w'\chi'}$, and an azimuthally averaged phase spectrum, $\bar{\Phi}_{w\chi}(K)$. One may further define normalized spectral energy and cospectrum as, $\tilde{E}_{w|n}(K) = \frac{\tilde{E}_w(K)}{\overline{w'^2}}$, $\tilde{E}_{\chi|n}(K) = \frac{\tilde{E}_\chi(K)}{\overline{\chi'^2}}$, $\tilde{C}_{w\chi|n}(K) = \frac{\tilde{C}_{w\chi}(K)}{\overline{w'\chi'}}$, which provide a quantitative measure of the individual contributions of motions with different wavenumbers to the total variance $\overline{w'^2}$, $\overline{\chi'^2}$ and flux $\overline{w'\chi'}$ in percentage. In this study, to calculate the azimuthally integrated spectral energy and cospectrum and azimuthally averaged phase spectrum, the 2D-FFT determined spectral energy, cospectra, and phase spectra, $E_w(k,l)$, $E_\chi(k,l)$, $C_{w\chi}(k,l)$ and $\Phi_{w\chi}(k,l)$, on a 2D plane are binned into the discretized total wavenumber indices, K, from 1 to 212 with an incremental of 1. All wavenumber indices greater than 212 are grouped into 212.

References

Arakawa, A., and W. H. Schubert (1974), Interaction of a cumulus cloud ensemble with the large-scale environment, Part I, *J. Atmos. Sci.*, *31*, 674–701, doi:10.1175/1520-0469(1974)031<0674:IOACCE>2.0.CO;2.

Asai, T. (1970), Stability of plane parallel flow with variable vertical shear and unstable stratification, *J. Meteorol. Soc. Jpn.*, *48*, 129–139.

Asai, T., and I. Nakasui (1973), The stability of Ekman boundary flow with thermally unstable stratification, *J. Meteorol. Soc. Jpn.*, *51*, 29–42.

Bender, M. A., I. Ginis, and Y. Kurihara (1993), Numerical simulations of tropical cyclone-ocean interaction with a high resolution coupled model, *J. Geophys. Res.*, *98*, 23,245–23,263.

Brown, R. A. (1980), Longitudinal instabilities and secondary flows in the planetary boundary layer: A review, *Rev. Geophys.*, *18*, 683–697.

Brümmer, B. (1985), Structure, dynamics and Energetics of boundary layer roll from KonTur Aircraft Observations, *Contrib. Atmos. Phys.*, *58*, 237–254.

Busch, N. E. (1973), The surface boundary layer' (Part I), *Boundary Layer Meteorol.*, *4*, 213–240.

Chen, S. S., and M. Curcic (2015), Ocean surface waves in Hurricane Ike (2008) and Superstorm Sandy (2012), Coupled modeling and observations, *Ocean Modell.*, doi:10.1016/j.ocemod.2015.08.005, in press.

Chen, S. S., W. Zhao, M. A. Donelan, and H. L. Tolman (2013), Directional wind-wave coupling in fully coupled atmosphere-wave-ocean models: Results from CBLAST-Hurricane, *J. Atmos. Sci.*, *70*, 3198–3215.

Chen, Y., and M. K. Yau (2001), Spiral bands in a simulated hurricane. Part I: Vortex Rossby wave verification, *J. Atmos. Sci.*, *58*, 2128–2145.

Deardorff, J. (1970), A numerical study of three-dimensional turbulent channel flow at large Reynolds numbers, *J. Fluid Mech.*, *41*(2), 453–480, doi:10.1017/S0022112070000691.

Deardorff, J. W. (1972), Numerical investigation of neutral and unstable planetary boundary layers, *J. Atmos. Sci.*, *29*, 91–115.

Donelan, M. A., M. Curcic, S. S. Chen, and A. K. Magnusson (2012), Modeling waves and wind stress, *J. Geophys. Res.*, *117*, C00J23, doi:10.1029/2011JC007787.

Dudhia, J. (1989), Numerical study of convection observed during the winter monsoon experiment using a mesoscale two-dimensional model, *J. Atmos. Sci.*, *46*, 3077–3107, doi:10.1175/1520-0469(1989)046<3077:NSOCOD>2.0.CO;2.

Etling, D. (1971), The stability of an Ekman boundary flow as influenced by thermal stratification, *Contrib. Atmos. Phys.*, *44*, 168–186.

Etling, D., and R. A. Brown (1993), Roll vortices in the planetary boundary layer: A review, *Boundary Layer Meteorol.*, *65*, 5–248.

Faller, A. J. (1961), An experimental analogy to and proposed explanation of hurricane spiral rainbands. Preprints, in *Second Technical Conference on Hurricanes*, pp. 307–313, Am. Meteorol. Soc., Miami, Fla.

Faller, A. J., and R. E. Kaylor (1966), A numerical study of the laminar Ekman layer, *J. Atmos. Sci.*, *23*, 466–480.

Foster, R. C. (2005), Why rolls are prevalent in the hurricane boundary layer, *J. Atmos. Sci.*, *62*, 2647–2661.

Gall, R. G., J. Tuttle, and P. Hildebrand (1998), Small-scale spiral bands observed in hurricanes Andrew, Hugo, and Erin, *Mon. Weather Rev.*, *126*, 1749–1766.

Grossmann, R. L. (1982), An analysis of vertical velocity spectra obtained in the BOMEX fair-weather, trade-wind boundary layer, *Boundary Layer Meteorol.*, *23*, 323–342.

Hong, S.-Y., and J. Dudhia (2003), Testing of a new non-local boundary layer vertical diffusion scheme in numerical weather prediction applications, paper presented at 20th Conference on Weather Analysis and Forecasting and 16th Conference on Numerical Weather Prediction, Amer. Meteorol. Soc., Seattle, Wash.

Kaimal, J., J. C. Wyngaard, Y. Izumi, and O. R. Cote (1972), Spectral characteristics of surface layer turbulence, *Q. J. R. Meteorol. Soc.*, *98*, 563–598.

Kaimal, J. C., J. C. Wyngaard, D. A. Haugen, O. R. Cote, Y. Izumi, S. J. Caughey, and C. J. Readings (1976), Turbulence structure in the convective boundary layer, *J. Atmos. Sci.*, *33*, 2152–2169.

Katsaros, K. B., P. W. Vachon, P. G. Black, P. P. Dodge, and E. W. Uhlhorn (2000), Wind fields from SAR: Could they improve our understanding of storm dynamics?, *John Hopkins APL Tech. Dig.*, *211*, 86–93.

Kelly, R. E. (1977), The onset and development of Rayleigh-Benard convectionin shear flows: A review, in *Physicochemical Hydrodynamics*, edited by B. B. Spalding, pp. 65–79, Adv. Publ., London, U. K.

Lee, C.-Y., and S. S. Chen (2012), Symmetric and asymmetric structures of hurricane boundary layer in coupled atmosphere-wave-ocean models and observations, *J. Atmos. Sci.*, *69*, 3576–3594.

Lee, C. Y., and S. S. Chen (2014), Stable boundary layer and its impact on tropical cyclone structure in a coupled atmosphere–ocean model, *Mon. Weather Rev.*, *142*, 1927–1944.

Lilly, D. K. (1966), On the instability of Ekman boundary layer flow, *J. Atmos. Sci.*, *23*, 481–494.

Mlawer, E. J., S. J. Taubman, P. D. Brown, M. J. Iacono, and S. A. Clough (1997), Radiative transfer for inhomogeneous atmosphere: RRTM, a validated correlated-k model for the longwave, *J. Geophys. Res.*, *102*, 16,663–16,682, doi:10.1029/97JD00237.

Morrison, I., S. Businger, F. Marks, P. Dodge, J. A., Businger (2005), An observational case for the prevalence of roll vortices in the hurricane boundary layer, *J. Atmos. Sci.*, *62*, 2662–2673.

Sakaida, F., H. Kawamura, and Y. Toba (1998), Sea surface cooling caused by typhoons in the Tohuku area in August 1989, *J. Geophys. Res.*, *103*, 1053–1065.

Scalise, K. (2013), Atmospheric distributions of polycyclic aromatic hydrocarbons (PAHs) in coastal Northern Gulf of Mexico, USA, associated with the deepwater horizon oil spill, Master's thesis, East Carolina Univ., Greenville, N. C.

Skamarock, W., J. B. Klemp, J. Dudhia, D. O. Gill, D. M. Barker, M. Duda, X. Y. Huang, and W. Wang (2008), A description of the advanced research WRF version 3, *NCAR Tech. note NCAR/TN/u2013475+ STR*, Mesoscale and Microscale Meteorology Division, NCAR, Boulder, Colo., doi:10.5065/D68S4MVH.

Thompson, G., R. M. Rasmussen, and K. Manning (2004), Explicit forecasts of winter precipitation using an improved bulk microphysics scheme. Part I: Description and sensitivity analysis, *Mon. Weather Rev.*, *132*, 519–542, doi:10.1175/1520-0493(2004)132<0519:EFOWPU>2.0.CO;2.

Thompson, G., P. R. Field, R.M. Rasmussen, and W. D. Hall (2008), Explicit forecasts of winter precipitation using an improved bulk microphysics scheme. Part II: Implementation of a new snow parameterization, *Mon. Weather Rev.*, *136*, 5095–5115.

Walker, N. D., and R. R. Leben (2005), Hurricane-forced upwelling and chlorophyll a enhancement within cold-core cyclones in the Gulf of Mexico, *Geophys. Res. Lett.*, *32*, L18610, doi:10.1029/2005GL023716.

Wallcraft, A. J., E. J. Metzger, and S. N. Carroll (2009), Software design description for the HYbrid Coordinate Ocean Model (HYCOM) version 2.2, *NRL Report NRL/MR/7320–09-9166*. Naval Research Laboratory, Stennis Space Center, Miss.

Walter, B. A., and J. E. Overland (1984), Observations of longitudinal rolls in a near neutral atmosphere, *Mon. Weather Rev.*, *112*, 200–208.

Wang, Y. (2002), Vortex Rossby waves in a numerically simulated tropical cyclone. Part II: The role in tropical cyclone structure and intensity changes, *J. Atmos. Sci.*, *59*, 1239–1262.

Wurman, J., and J. Winslow (1998), Intense sub-kilometer-scale boundary layer rolls observed in Hurricane Fran, *Science*, *280*, 555–557.

Zhu, P. (2008a), A multiple scale modeling system for coastal hurricane wind damage mitigation, *Nat. Hazards*, *47*(3), 577–591, doi:10.1007/s11069-008-9240-8.

Zhu, P. (2008b), Simulation and parameterization of the turbulent transport in the hurricane boundary layer by large eddies, *J. Geophys. Res.*, *113*, D17104, doi:10.1029/2007JD009643.

Zhu, P., B. A. Albrecht, V. P. Ghate, and Z.-D. Zhu (2010), Multiple scale simulations of stratocumulus clouds, *J. Geophys. Res.*, *115*, D23201, doi:10.1029/2010JD014400.